ACS Catalysis

pubs.acs.org/acscatalysis Research Article

Tailoring Metal-Ion-Doped Carbon Nitrides for Photocatalytic Oxygen Evolution Reaction

Shanping Liu, Valentin Diez-Cabanes, Dong Fan, Lu Peng, Yuanxing Fang, Markus Antonietti,* and Guillaume Maurin*

Cite This: *ACS Catal.* 2024, 14, 2562−2571 Read Online

ACCESS | Metrics & More | Article Recommendations | Supporting Information

ABSTRACT: Poly(heptazine imides) (PHIs) have emerged as prominent layered carbon nitride-based materials with potential oxygen evolution reaction (OER) catalytic activity owing to their strong VIS light absorption, long excited-state lifetimes, high surface-to-volume ratios, and the possibility of tuning their properties via hosting different metal ions in their pores. A series of metal-ion-doped PHI-M (M = K^+, Rb^+, Mg^{2+}, Zn^{2+}, Mn^{2+}, and Co^{2+}) were first systematically explored using density functional theory calculations. These simulations led an in-depth understanding of the microscopic OER mechanism in these systems and identified PHI-Co^{2+} as the best OER catalyst of this family of PHIs, whereas PHI-Mn^{2+} can be an alternative promising OER catalyst. This level of performance was attributed to a thermodynamically favorable formation of the reaction intermediates as well as its red-shifted absorption in the VIS region involving the population of long-lived states, as revealed by time-dependent density functional theory calculations. We further demonstrated that the electronic properties of the *OH intermediates (Bader population, crystal orbital Hamilton population analysis, and adsorption energies) are reliable descriptors to anticipate the OER activity of this family of PHIs. This rational analysis paved the way toward the prediction of the OER performance of another PHI-M derivative, i.e., PHI-Fe^{2+}. The computationally explored PHI-Fe^{2+}, PHI-Mn^{2+}, and PHI-Co^{2+} systems were then synthesized alongside PHI-K^+, and their photocatalytic OER activities were assessed. These experimental findings confirmed the best photocatalytic OER performance for PHI-Co^{2+} with an oxygen production of 31.2 $\mu mol \cdot h^{-1}$ that is 60 times higher than the pristine g-C_3N_4 (0.5 $\mu mol \cdot h^{-1}$), whereas PHI-Fe^{2+} and PHI-Mn^{2+} are seen as alternative OER catalysts with attractive oxygen production of 11.20 and 4.69 $\mu mol \cdot h^{-1}$, respectively. Decisively, this joint experimental−computational study reveals PHI-Co^{2+} to be among the best of the OER catalysts so far reported in the literature including some perovskites.

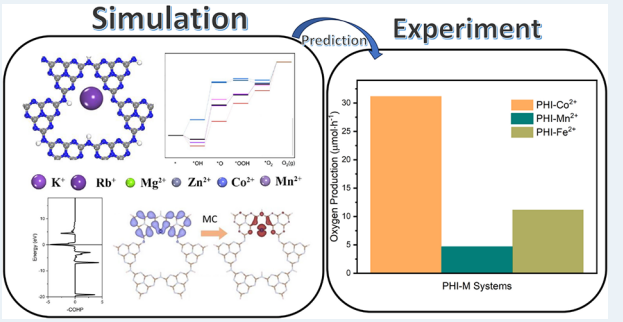

KEYWORDS: *PHIs, OER catalysts, simulations, experiments, performance*

INTRODUCTION

Photocatalysis represents an attractive and promising process to address the current environmental and energy supply global issues. Its capability to convert solar green energy into storable chemical fuels offers a unique opportunity to develop a sustainable energy economy.[1,2] Photocatalytic water splitting is considered as one of the most effective approaches for producing high-purity H_2, a future eco-friendly source of clean energy, using renewable sources.[3] Three steps are involved in the overall water-splitting process: light-harvesting, electron/charge generation, and catalytic reaction.[3] TiO_2 and its derivatives have been demonstrated to photoinduce water splitting,[4] and they have been largely explored as photoactive semiconductors until these days. However, the large band gap exhibited by TiO_2 (∼3.2 eV) represents a major factor limiting its efficiency because it absorbs light in the UV region, which represents only 4% of the solar light spectrum. In this context, many new candidates have emerged over the last years aiming to boost the light harvesting capacity of the semiconductor materials via shifting the absorption energy windows to the VIS region (1.6−3.2 eV), as it is typically the case with ZnO,[5] Cu_2O,[6] CdS,[7] $SrTiO_3$,[8] or $BiVO_4$,[9] among others.

Interestingly, in 2009, Wang et al. evidenced that graphitic carbon nitride (g-C_3N_4) materials can be effective photocatalysts for water splitting, representing a major breakthrough in the field by shifting the attention to two-dimensional (2D) material catalysts.[10] Compared to their 3D-counterparts, 2D materials potentially display an enhanced photoactivity due to several advantages, e.g., large surface-to-volume ratio, which

Received: December 7, 2023
Revised: January 19, 2024
Accepted: January 24, 2024
Published: February 2, 2024

https://doi.org/10.1021/acscatal.3c05961
ACS Catal. 2024, 14, 2562−2571

enhances the solar light collection and the surface area exposed to reaction; high tunability of their optoelectronic properties via layer engineering; and the unique opportunity to enhance the charge separation and to increase the concentration of active sites owing to their layered geometry.[11] In particular, g-C_3N_4 exhibits strong absorption in the VIS region (band gap of 2.7 eV) and high stability under extreme conditions owing to the π-conjugation of its sp^2-hybridized carbon and nitrogen atoms.[12,13] These favorable features made this family of 2D materials attractive for many photocatalytic reactions including CO_2 reduction and abatement of many contaminants.[14,15] However, the pristine g-C_3N_4 still presents some drawbacks limiting its photocatalytic performance, including a poor electronic conductivity and a rather high recombination of photogenerated electron−hole pairs.[16] Different strategies have been envisaged to overcome these limitations, e.g., defect engineering,[17−19] doping by different metal or nonmetal elements to tune the electronic properties,[20−23] or co-catalyst integration via the construction of heterojunctions.[24,25]

Alternatively, modulating the patterns of the g-C_3N_4 structure was also revealed as an effective strategy to further improve the photocatalytic performance of this system.[26−28] Typically, the prototypical g-C_3N_4 melon units can be recrystallized in salt melts to produce highly condensed C_3N_4 patterns, known as poly(heptazine imides) (PHIs), characterized by a fully delocalized π-electron system linked by an imide bridge.[26] As a result, PHIs have been explored for several photocatalytic reactions, e.g., rhodamine B degradation[29] and oxidation of benzyl alcohol to benzaldehyde,[30] among others.[31−34] Notably, the available porosity and the fully delocalized π-electron of the PHI structure enable hosting doping metal ions in a well-patterned fashion.[35] Moreover, when combined with electron donor groups, PHIs can be photoproduced into long-lived radicals, essential for triggering the reactions and enabling the development of time-delayed discharge after illumination.[36] Dontsova et al. synthesized in 2015 the first potassium-ion-doped PHI (PHI-K^+) by pyrolysis of 3,5-disubstituted-1,2,4-triazole derivatives in LiCl/KCl eutectics; however, it showed identical photophysical properties to those of mpg-CN.[37] Other PHI-M (M = Li^+, Na^+, Cs^+, Ag^+, Ca^{2+}, Zn^{2+}, Mg^{2+}, Fe^{2+}, Co^{2+}, Ni^{2+}, Au^{3+}, Ru^{3+}) derivatives have been then prepared following a similar synthetic route and further tested for hydrogen evolution reaction (HER).[38−41] Compared to HER, the second half-reaction, i.e., oxygen evolution reaction (OER) required to complete the overall water splitting process, is by far more challenging because it involves an intricate four-electron transfer ($4OH^- \rightarrow 2H_2O + O_2 + 4e^-$) that is much less kinetically favorable. So far, noble-metal-based oxides such as RuO_2 and IrO_2 have been reported as the best OER photocatalysts;[42−44] however, because of their high cost and limited resources, there is a critical need to search for alternative OER catalysts. As a prominent photoactive material, perovskite also exhibits an attractive OER performance.[45] The large majority of the other studies focused on layered double hydroxides and metal−organic Frameworks as OER electrocatalysts.[46,47] The Co^{2+}/K^+-co-doped PHIs have been equally evoked as potential OER electrocatalysts with Co^{2+} as the active site;[48] however, we are not aware of any studies on the potential use of PHIs for photocatalytic OER.

From a theoretical standpoint, a few first-principles molecular simulation studies were reported on the structural and optoelectronic properties of PHI derivatives. Typically, Savateev et al. performed periodic density functional theory (DFT) calculations to analyze the band edges of PHI-K^+ and their absorption properties in the near-infrared region.[32] Partial O-doping of the PHI structure was also predicted to boost the VIS light absorption of this family of materials.[49] Kühne et al. performed the same level of calculations to explore the HER activity of PHIs. PHI-Mg^{2+} was predicted as the most effective HER catalyst but with only a tiny enhancement of the catalytic activity as compared to the pristine material (PHI-H).[39]

Notably, there is a clear lack of understanding/rational analysis of the key factors of PHI derivatives, e.g., their electronic properties, reaction thermodynamics, light harvesting, and charge transfer behaviors that govern their catalytic activities. Furthermore, the properties of their excited states have never been computationally explored. This hinders overall the development of PHI-M systems with improved catalytic activities.

In this regard, herein a joint theoretical−experimental effort was devised to systematically assess the optoelectronic and thermodynamical properties of a series of metal-ion-doped PHI materials, alongside their OER activities. More specifically, DFT and time-dependent DFT (TD-DFT) calculations were deployed to explore the promises of a series of PHI-M (M = K^+, Rb^+, Mg^{2+}, Zn^{2+}, Co^{2+}, and Mn^{2+}) for OER based on the analysis of their simulated energetic alignments, stabilities of their reaction intermediates, and their absorption characteristics. We further identified the relevant descriptors of the PHI-M that govern their optoelectronic properties and OER activities. PHI-Co^{2+} was predicted as the best OER catalyst owing to an extension of the absorption energy region compared to the other PHI-M, as well as to the population of long-lived charge separated states upon VIS light irradiation. The electronic properties of the *OH intermediates, i.e., Bader population, crystal orbital Hamilton population (COHP) analysis, and adsorption energies, were identified as the most reliable descriptors to describe the OER performance of this family of PHIs. This rational analysis paved the way toward the exploration of an alternative PHI-M system, PHI-Fe^{2+}, with an OER activity predicted to be similar to PHI-Mn^{2+} although much less attractive than PHI-Co^{2+}. These predicted metal ion doped PHIs were further synthesized alongside PHI-K^+ for comparison and tested as OER catalysts. In line with the computational findings, PHI-Co^{2+} was demonstrated to exhibit the highest oxygen production performance (31.20 μmol·h^{-1}), whereas PHI-Fe^{2+} and PHI-Mn^{2+} showed promising activity (11.20 and 4.69 μmol·h^{-1} respectively), this level of performance surpassing by far that of the pristine g-C_3N_4 (0.5 μmol·h^{-1}).[50]

METHODS

Computational Methods. The initial computational screening of the OER activity of the PHI-M systems was performed by considering a periodic single PHI layer model (cell dimension a = 21.4 Å and b = 12.4 Å and vacuum of 20 Å in the c direction, as shown in Figure S1) containing one metal cation, i.e., 4.8, 9.9, 3.0, 7.7, 7.2, and 6.6 wt % for K^+, Rb^+, Mg^{2+}, Zn^{2+}, Co^{2+}, and Mn^{2+}, respectively, that reasonably covers the concentration range attainable experimentally for these systems (Figure 1).[51] The PHI-H model incorporates three hydrogen atoms to achieve a neutral system. In the case of metal-cation-doped systems, the hydrogen atoms are substituted accordingly. For instance, one hydrogen atom was replaced by a K^+ cation to create PHI-K^+, and two

https://doi.org/10.1021/acscatal.3c05961
ACS Catal. 2024, 14, 2562−2571

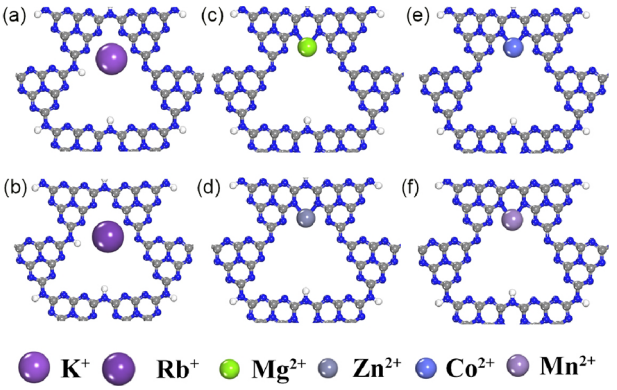

Figure 1. DFT-optimized geometries of the single-layer PHI-M models: (a) PHI-K^+, (b) PHI-Rb^+, (c) PHI-Mg^{2+}, (d) PHI-Zn^{2+}, (e) PHI-Co^{2+}, and (f) PHI-Mn^{2+}.

hydrogen atoms were substituted by one Co^{2+} ion to form PHI-Co^{2+}; the same approach was followed for the remaining systems.[39] All periodic DFT calculations were carried out by adopting projector augmented wave (PAW) pseudopotentials as implemented in the Vienna Ab initio Simulation Package (VASP) code.[52,53] The atomistic positions were relaxed within the generalized gradient approximation (GGA) Perdew–Burke–Ernzerhof (PBE) functional for both exchange and correlation parts,[54] whereas Grimme's D3 dispersion method was adopted to take into account the van der Waals interactions.[55] We applied a Hubbard correction to account for the pronounced correlation in the unfilled *d* orbitals with U = 5.3, 3.9 and 3.32 for Fe, Mn, and Co, respectively.[56] The Kohn–Sham orbitals were expanded in a plane-wave basis set with an energy cutoff of 550 eV. The Brillouin zone was sampled by following a Monkhorst–Pack scheme with a 2 × 3 × 1 *k*-point grid. For the geometry optimization, all atomic positions were fully relaxed until they reached a convergence criterion equal to 10^{-5} eV and 0.01 eV/Å for the energies and forces, respectively. The zero-point energy (ZPE) and entropy correction at T = 298 K obtained from the vibrational frequencies were considered for each intermediate to assess the Gibbs free energy with the configuration of free intermediate and totally constrained PHI-M (Table S1).[57] The electronic structures of all DFT-optimized PHI-M structures were assessed by employing different types of DFT implementations, i.e., pure (PBE), meta-GGA (SCAN), and hybrid (HSE) functionals.[58,59]

We defined the adsorption energy (E_{ads}) for each intermediate species as follows:

$$E_{ads} = E_{total} - E_{PHI\text{-}M} - E_{intermediate}$$

where E_{total} is the total energy of the adsorptive system, $E_{PHI\text{-}M}$ is the energy of metal-doped PHI, and $I_{intermediate}$ is the energy of the isolated intermediate species.

Bader charge population analysis was performed by using the program developed by Henkelman' group.[60] The LOSTER program was used to study the COHP, which gave us access to a precise description of the interactions between PHI-M and *OH intermediate species.[61] Finally, the excited-state properties of PHI-M were investigated by performing TD-DFT on the reduced cluster models depicted in Figure S2. We relied on the simplified TD-DFT (sTD-DFT) scheme to study PHI-M (M = K^+, Rb^+, Mg^{2+}, Zn^{2+}, Co^{2+}, Mn^{2+}, and Fe^{2+}), and the best OER predicted catalysts were further analyzed by employing the full TD-DFT implementation.[62] More details about the TD-DFT calculations and the cluster models can be found in the Supporting Information (SI). All the details of the preparation, characterization, and photocatalytic tests of PHI-M are described in the SI.

RESULTS AND DISCUSSION

Systematic Exploration of the Structural/Electronic Properties and OER Activities of PHI-M (M = K^+, Rb^+, Mg^{2+}, Zn^{2+}, Co^{2+}, and Mn^{2+}). Figure 1 shows the top view for all the DFT-geometry optimized PHI-M structures. Interestingly, K^+ and Rb^+ cations remain located in the center of the pore (the narrowest N–M distance range from 2.58 to 2.71 Å) associated with weak interactions with the PHI atoms. In contrast, the other metal ions are preferentially localized next to the charged nitrogen atoms of the PHI layer (M–N distances ranging from 2.01 to 2.11 Å). This distinct behavior is in line with the sequence of the cationic radius of these metals, with the smaller cations being able to be closer to the PHI atoms.

From these DFT-geometry optimized structures, we further evaluated the impact of cation doping on the electronic structure of PHI-M. Table 1 shows that the band gap

Table 1. Simulated Band Gaps (eV) for the Series of Metal-Ion-Doped PHI-M Systems Using Different DFT Functionals

functional	PHI-H	PHI-K^+	PHI-Rb^+	PHI-Mg^{2+}	PHI-Zn^{2+}	PHI-Co^{2+}	PHI-Mn^{2+}
PBE	1.93	0.85	1.00	1.38	0.92	1.59	1.39
SCAN	2.29	1.19	1.33	1.71	1.05	1.93	1.72
HSE	3.51	2.57	2.71	3.02	2.57	3.14	3.03

computed using the PBE functional (Figure S4) for the pristine PHI-H (1.93 eV) underestimates the experimental band gap (2.7 eV),[37] thus lying in the deviation of 30–40% generally obtained with this functional for the band gap of a wide range of materials.[63] The use of the meta-GGA SCAN functional led to a band gap of 2.29 eV for PHI-H, approaching the experimental value (Figure S4). In contrast, the HSE computed gaps yielded 3.5 eV, in line with previous calculations conducted with the same functional (3.2 eV),[64] which is higher than the experimental value (2.7 eV). Lei et al. demonstrated that the band gap of mesh-like graphic carbon nitride narrows gradually with increasing temperature, which might explain the discrepancy between experimental and simulated values. They attributed these changes to the rising condensation degree leading to an improved π-electron delocalization in the conjugated heptazine systems.[64] However the HSE hybrid functional (Figure 2) enabled to describe much better the experimental band gap of PHI-K^+ (2.57 vs 2.68 eV) compared to SCAN (1.19 eV).[39] These overall calculations further revealed that the metal cation doping results in a band gap reduction, which is larger for the alkali metals (K^+ and Rb^+). This observation is attributed to a destabilization of the valence band (VB) edges due to the localization of holes around the N atoms surrounding the doping metal (Figure S5), whereas the conduction band (CB) states remain mostly unaltered. PHI-Zn^{2+} shows the lowest CB position with a main contribution of its filled *d* orbitals as shown in Figure S6. Regarding the absolute energetic alignment, Figure 2 shows the band edge positions for all

https://doi.org/10.1021/acscatal.3c05961
ACS Catal. 2024, 14, 2562–2571

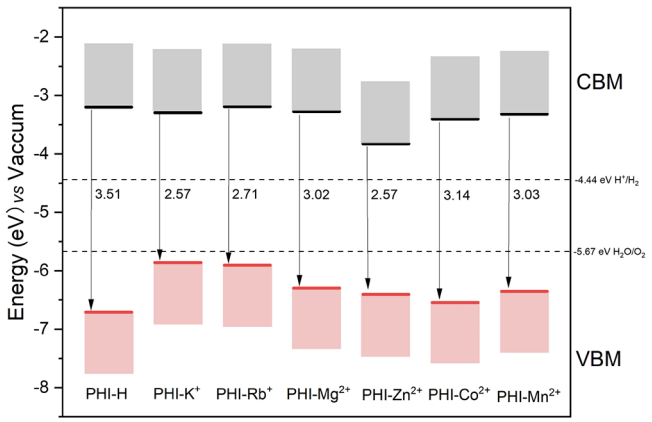

Figure 2. Conduction band minimum (CBM) and valence band maximum (VBM) positions vs vacuum simulated at the DFT level for all PHI-M systems using the HSE functional.

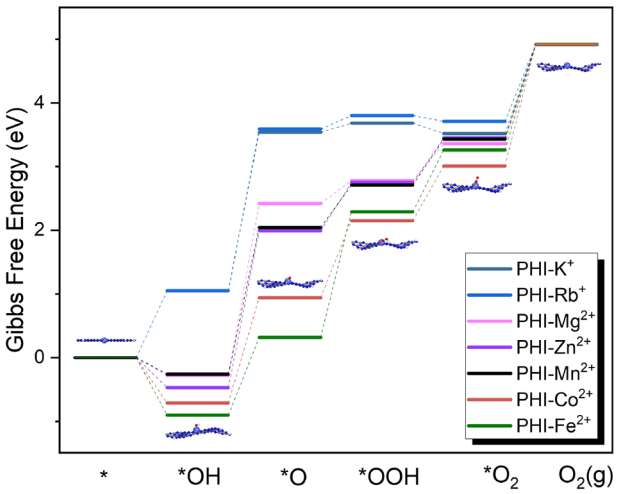

Figure 3. Simulated OER pathways for the series of metal-ion-doped PHI-M systems. The geometries for the intermediates obtained for the PHI-Co^{2+} system are illustrated. The geometries for the intermediates of the other PHI-M systems are shown in Figure S6. All of the detailed data are shown in Table S2.

investigated PHI-M systems computed at the HSE level. Notably, the calculated CB and VB edge energies for the pristine PHI-H are −3.2 and −6.7 eV, respectively (Figure 2), are in good agreement with the corresponding experimental values reported in the literature (−3.5 and −6.4 eV, respectively).[39] More importantly, all the VB edges lie below the O_2 oxidation (−5.67 V vs vacuum), suggesting a thermodynamically favorable effective hole and electron injection for Mg^{2+}, Zn^{2+}, Co^{2+}, and Mn^{2+} doped PHIs but unfavorable for K^+ and Rb^+ doped PHIs since the VBM is located at a higher relative energy (Figure 2).

Because all these metal-ion-doped PHI systems possess a suitable energetic alignment to promote photogenerated charges for the catalytic reaction, we further focused our attention on the energetics that drive the OER pathways. To this end, we relied on a conventional adsorbate evolution mechanism where the O−O bond forms throughout the oxyhydroxide species (MOOH),[65] with the consideration of a final adsorbed $*O_2$ desorption step to mimic the reaction conditions. This reaction scheme implies the adsorption of reactants and both the formation and release of the product. Thus, the complete reaction pathway can be defined as follows:

$$* + H_2O \rightarrow {}^*OH + H^+ + e^-$$

$$^*OH \rightarrow {}^*O + H^+ + e^-$$

$$^*O + H_2O \rightarrow {}^*OOH + H^+ + e^-$$

$$^*OOH \rightarrow {}^*O_2 + H^+ + e^-$$

$$^*OOH \rightarrow {}^*O_2 + H^+ + e^-$$

$$^*O_2 \rightarrow * + O_2(g)$$

The asterisk (*) denotes the adsorbed states. The calculated free Gibbs energies of each intermediate of the OER pathway for all metal-ion-doped PHIs are reported in Figure 3. This figure evidences that the nature of the metal ions affects substantially the energy of all intermediates and therefore modulates the rate-determining step (RDS) of the reaction pathway. For instance, for PHI-K^+ and PHI-Rb^+ systems, the RDS is the dehydrogenation of the initial OH* absorbate, with reaction energies equal to 2.49 and 2.54 eV for *O and *OH intermediates, respectively. These doped PHIs thus display less stable intermediates and larger overpotentials, thus triggering their practical application as OER catalysts. This computational finding is consistent with previous works reporting poor OER electrocatalytic activities achieved by PHI-K^+.[39] The RDS for PHI-Mg^{2+}, PHI-Zn^{2+} and PHI-Mn^{2+} is the dehydrogenation of *OH with corresponding reaction energies of 2.70 2.46, and 2.30 eV, respectively. Despite showing improved stabilization of the intermediates compared to PHI-K^+ and PHI-Rb^+, their associated reaction energies are still rather high. Finally, the RDS for PHI-Co^{2+} is the desorption of adsorbed $*O_2$ with reaction energies of 1.91 eV. The lower reaction energy as compared to the values obtained for the other doped PHIs together with the high stability of its reaction intermediates suggests a rather good OER activity. These overall theoretical findings deliver a first confirmation of the attractiveness of PHI-Co^{2+} for the electrochemical OER experimentally reported earlier.[48]

Figure 3 highlights that we can split the series of metal-cation-doped PHIs into three categories depending on the energy needed to initialize the OER process, i.e., the OH absorption at the metal ion site: (i) for PHI-K^+ and PHI-Rb^+, this is an endothermic process with reaction energies of 1.05 and 1.05 eV, respectively, (ii) for PHI-Mg^{2+}, PHI-Zn^{2+}, and PHI-Mn^{2+}, the reaction is exothermic with intermediate formation energies of −0.28, −0.47, and −0.26 eV, respectively; and (iii) for PHI-Co^{2+}, this step is highly exothermic with a reaction energy of −0.71 eV. As a general trend, the thermodynamics driving the formation of the *OH absorbate governs the OER performance of PHI-M. Therefore, the electronic properties of the *OH intermediate can be envisaged as valuable descriptors of the overall OER activities achieved by this family of materials.

Identification of Key PHI-M Descriptors for OER Activity. Following the suggestions mentioned above that the *OH intermediate plays a key role in the OER activity of PHI-M, we carefully examined certain properties of the *OH intermediate to identify relevant descriptors. First, we analyzed the resulting charge transfer upon *OH adsorption by means of the Bader charge population analysis (Table 2). Notably, this analysis evidenced that Mn^{2+} and Co^{2+} cations become

https://doi.org/10.1021/acscatal.3c05961
ACS Catal. 2024, 14, 2562−2571

Table 2. Bader Charge Changes of the Doping Metal Ions in the *OH Intermediate Compared to the Metal Ion in the Pristine PHI-M

PHI-M systems	changes of Bader charge (Δe^a)	adsorption energy of *OH (eV)
PHI-K^+	−0.0002	−2.32
PHI-Rb^+	−0.0032	−2.32
PHI-Mg^{2+}	0.0011	−3.66
PHI-Zn^{2+}	0.0610	−3.88
PHI-Mn^{2+}	0.0857	−3.67
PHI-Co^{2+}	0.0723	−4.11
PHI-Fe^{2+}	0.0893	−3.37

[a]Δe = e (Bader charge of metal ion in the *OH intermediate) − e (Bader charge of metal ion in the pristine PHI-M).

more negatively charged (0.08 and 0.07 e^-, respectively) upon the formation of the M-O bond for the *OH intermediate. This result is in line with the highest stability of the *OH intermediate for these two metal ions as highlighted by their highest calculated adsorption energies summarized in Table 2.

We further conducted COHP analysis between the doped metal ions and the oxygen atom of *OH (M-O) for all *OH adsorption configurations to gain insight into the origin of the adsorption energies reported in Table 2.[66] The corresponding COHP is plotted as a function of the band structure energy with respect to the Fermi level (Figure 4), where positive and

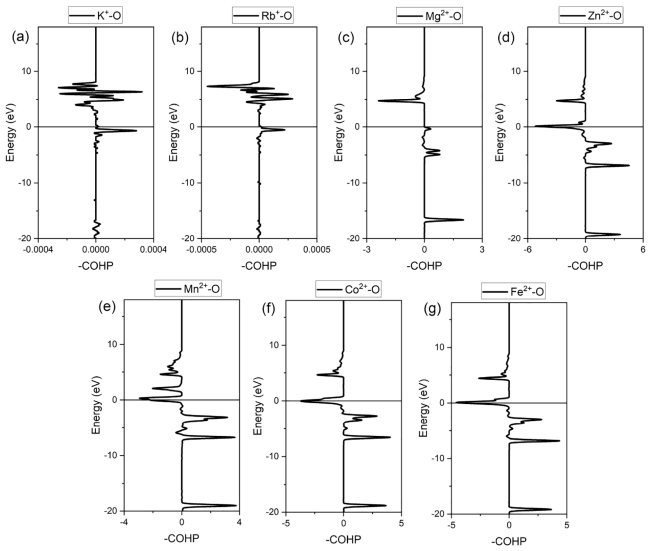

Figure 4. Crystal orbital Hamilton population (COHP) analysis of metal ion−oxygen interactions in *OH adsorption configuration for the different PHI-M systems. Zero Energy corresponds to the Fermi level. (a) PHI-K^+, (b) PHI-Rb^+, (c) PHI-Mg^{2+}, (d) PHI-Zn^{2+}, (e) PHI-Mn^{2+}, (f) PHI-Co^{2+}, and (g) PHI-Fe^{2+}.

negative values of −COHP correlate with bonding and antibonding interactions, respectively. The relative bond strength and degree of coupling between atom pairs were then obtained by the integration of −COHP (ICOHP) profiles. Our analysis revealed that PHI-Mn^{2+} (Figure 4e) and PHI-Co^{2+} (Figure 4f) possess the largest integration values in the energy range below the Fermi level, thus indicating a strong Mn−O and Co−O bonding strength at the origin of the high stabilities of the corresponding intermediates. In contrast, PHI-K^+ and PHI-Rb^+ (Figure 4a,b) exhibit the lowest −COHP integration value below the Fermi level, thus leading to poor coupling between *OH and the metal ions. The moderate integration values exhibited by PHI-Mg^{2+} and PHI-Zn^{2+} (Figure 4c,d) are consistent with moderate bond strength. Notably, the Co−O and Mn−O COHP profiles also show that the Fermi level lies within an antibonding interaction region, thus enhancing the interactions between *OH and the metal ions.

Descriptor Rationalization toward Prediction. As a further stage, we aimed to validate the reliability of the descriptors (Bader population, COHP analysis, and adsorption energies) to predict the OER activities of another PHI-M system. As a proof of concept, we opted for PHI-Fe^{2+}. We first revealed that the charge transfer induced by the formation of *OH on this metal site (Fe^{2+}) is rather high (0.089 e^-) and its corresponding calculated adsorption energy is −3.37 eV. On the same vein, the COHP analysis of the Fe−O pair within the *OH adsorption configuration evidenced a strong interaction between Fe^{2+} and O atoms for the *OH intermediate, which can be mainly ascribed to their bonding combination, whereas the Fermi level locates in an antibonding state region (Figure 4g). Overall, the PHI-Fe^{2+} OH* intermediate is reminiscent to its Mn^{2+} and Co^{2+} counterpart in terms of charge transfer and state hybridization.

With the objective of corroborating this hypothesis, we calculated the entire OER pathway for PHI-Fe^{2+} that was compared with that obtained for PHI-Co^{2+} and PHI-Mn^{2+} as displayed in Figure 3. The corresponding intermediate configurations are illustrated in Figures S7f. The RDS for PHI-Fe^{2+} is demonstrated to be the formation of *OH species within an energy barrier of 2.42 eV. This barrier is substantially higher compared to PHI-Co^{2+} (1.91 eV) and of the same order of magnitude as PHI-Mn^{2+} (2.30 eV). Having the same RDS and closely matching the energy barrier with PHI-Mn^{2+}, PHI-Fe^{2+} should exhibit comparable performance with PHI-Mn^{2+}, whereas it is predicted to be much less effective compared to PHI-Co^{2+}. Lastly, to check that the energetic alignment of PHI-Fe^{2+} is suitable to promote charges for OER, we also computed its electronic structure properties. Its calculated band gap is 3.29 eV employing the HSE functional, whereas its VB edge energy is located about −6.43 eV below the reference OER potential.

We have thus demonstrated that the OER catalytic behavior of a given PHI-M system can be anticipated by estimating the properties of the *OH intermediates, thus avoiding the need to calculate the full reaction pathway for each possible PHI-M candidate. This computational analysis pointed out that PHI systems doped with Co^{2+}, Fe^{2+} and Mn^{2+}, metal ions are the most prominent candidates for OER. These conclusions are based on a ground-state perspective without considering the action of light, thus neglecting important effects such as the interactions between the photogenerated charges (electron−hole pairs). To fill this gap, we have thus investigated the excited-state properties of the different doped PHI systems.

Excited-State Properties of PHI-M. We analyzed the photophysical behavior of the different PHI-M materials under light irradiation by means of TD-DFT calculations. We first computed their absorption spectra in the UV−vis region, as shown in Figure 5a, using cluster models depicted in Figure S2. Notably, the simulated spectrum of PHI-H displays its main absorption $\pi-\pi^*$ bands centered at ∼4.5 eV, showing very weak absorption bands below this energy. New absorption features appear in this energy window for all PHI-M that

https://doi.org/10.1021/acscatal.3c05961
ACS Catal. 2024, 14, 2562−2571

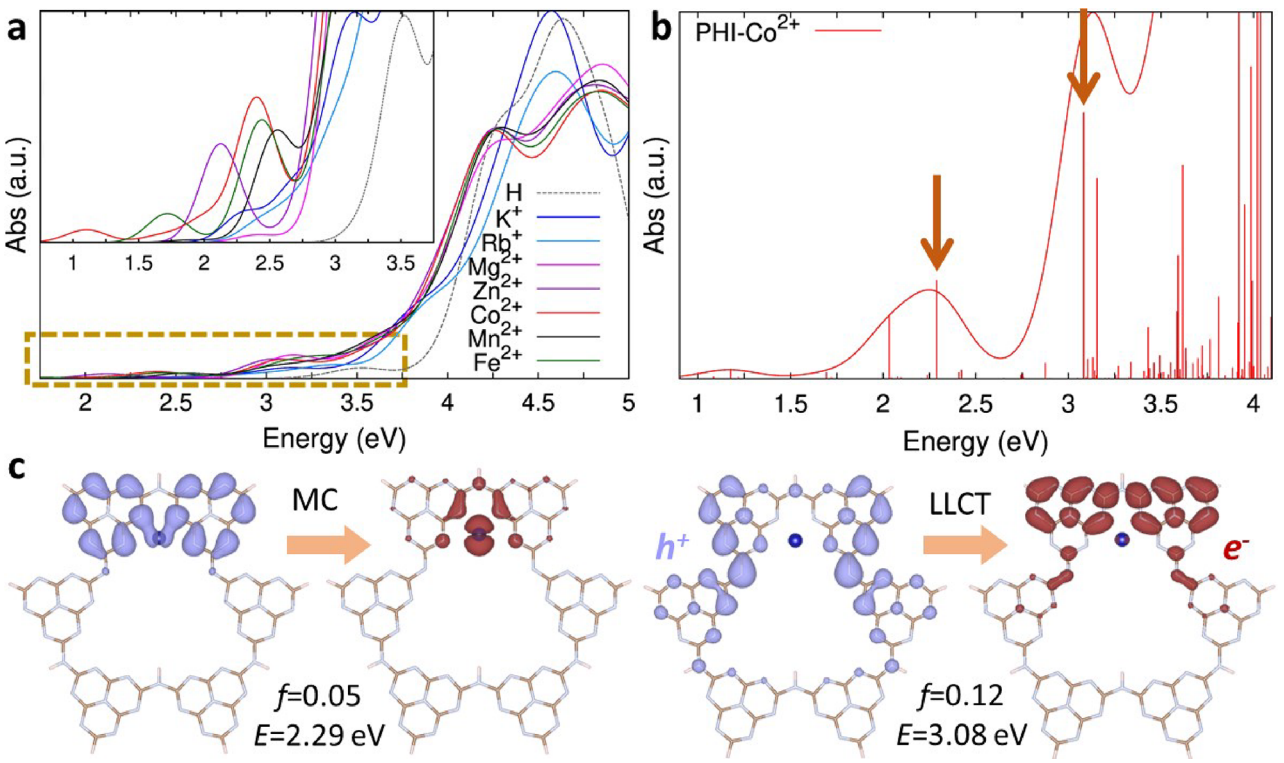

Figure 5. (a) Simulated absorption spectra for all doped PHI-M by TD-DFT calculations, where the reference PHI-H spectrum is depicted with dotted gray lines. The lowest energy region part of the spectra that is delimited by the yellow dashed lines is also plotted in the inset. (b) Simulated absorption spectrum of PHI-Co^{2+}. Vertical lines correspond to the states contributing to the spectra, and their intensities are related with the oscillator strengths. (c) NTO plots for the states of the PHI-Co^{2+} spectrum indicated by the orange arrows, together with their corresponding absorption energies and oscillator strengths. Purple/red colors are used to depict the occupied/virtual NTO isodensities. The isovalue density used in the plots was set to 0.02 au. The NTOs for the rest of the important states contributing to the PHI-Co^{2+} spectrum are represented in Figure S11.

depend on the charge of the metal cation (which dictates its symmetry) rather than their spin or electronic configurations. PHI-K^+ and PHI-Rb^+ show identical absorption spectra, with the $\pi-\pi^*$ bands remaining at the same position as for PHI-H, whereas a shoulder emerges at 3.5 eV. For the divalent metal-ion-doped PHI, $\pi-\pi^*$ absorption bands are red-shifted by 0.4 eV with respect to PHI-H, and interestingly, apart from the band shoulders displaying band edge energies of about 2.5 eV, new absorption features cover the lowest-energy region (>1 eV) for most of them except PHI-Mg^{2+} (see the inset of Figure 6a). Typically, PHI-Mn^{2+} and PHI-Zn^{2+} exhibit one absorption peak centered at 2.1 at 2.5 eV, respectively. Notably, the most prominent absorption features in the lowest energy region are obtained for PHI-Co^{2+} and PHI-Fe^{2+} with two absorption signals: one very weak at 1.2 and 1.7 eV and another one more intense centered at 2.3 and 2.5 eV, respectively, with PHI-Co^{2+} exhibiting the most intense absorption bands. The red-shift of the absorption features triggered by the highest oxidation state of the doping cation was further confirmed by periodic TD-DFT calculations (Figure S8), thus validating the choice of our cluster models to scan the full series of PHI-M. The existence of such low energy absorption bands may be originated from the DFT issues related with triplet instabilities.[67] Nevertheless, we demonstrated that the absorption signals in the energy region below the main $\pi-\pi^*$ band are present independently of the choice of the type of DFT functional implemented (Figures S9 and S10).

The energy red-shift of the absorption features simulated for the divalent metal cations PHI is expected to be correlated with their photocatalytic activities, the most pronounced shift being evidenced for the best predicted OER catalyst, i.e., PHI-Co^{2+}. The question is whether the population of the lowest energy states would lead to the generation of charges promoting the catalytic reaction or if they would recombine in a short time scale. To shed light on this, we investigated the charge separation for the lowest energy states of PHI-Co^{2+} displayed in Figure 5b by means of the natural transition orbital (NTO) analysis, which enables one to determine the spatial location of the photogenerated charges (holes/electrons) as represented in Figure 5c. For the states located in the lowest energy region (~ 2 eV or lower), both generated charges are locally confined on the metal ions, which would yield to an ultrafast deactivation of these states upon being populated. On the other hand, for the states corresponding to the absorption shoulder of the $\pi-\pi^*$ band (~ 3.1 eV), holes remain localized on the central aromatic cores of the considered cluster, whereas the electrons are delocalized around the PHI atoms surrounding the metal ions, thus conferring them a ligand-to-ligand charge transfer (LLCT) character that should hinder the charge recombination. Then, shifting to higher energies, one can find the $\pi-\pi^*$ states located at 4 eV, which are fully delocalized along the considered cluster (Figure S11). It is important to highlight that the nature of the states described above was found to be independent of the type of hybrid functionals employed (Figures S11 and S12). Overall, it shows that the improvement of the photoactivity of PHI-Co^{2+} originates from its enhanced light harvesting of red photons and to the population of long-lived charge separated states upon irradiation of the main absorption band edges.

https://doi.org/10.1021/acscatal.3c05961
ACS Catal. 2024, 14, 2562−2571

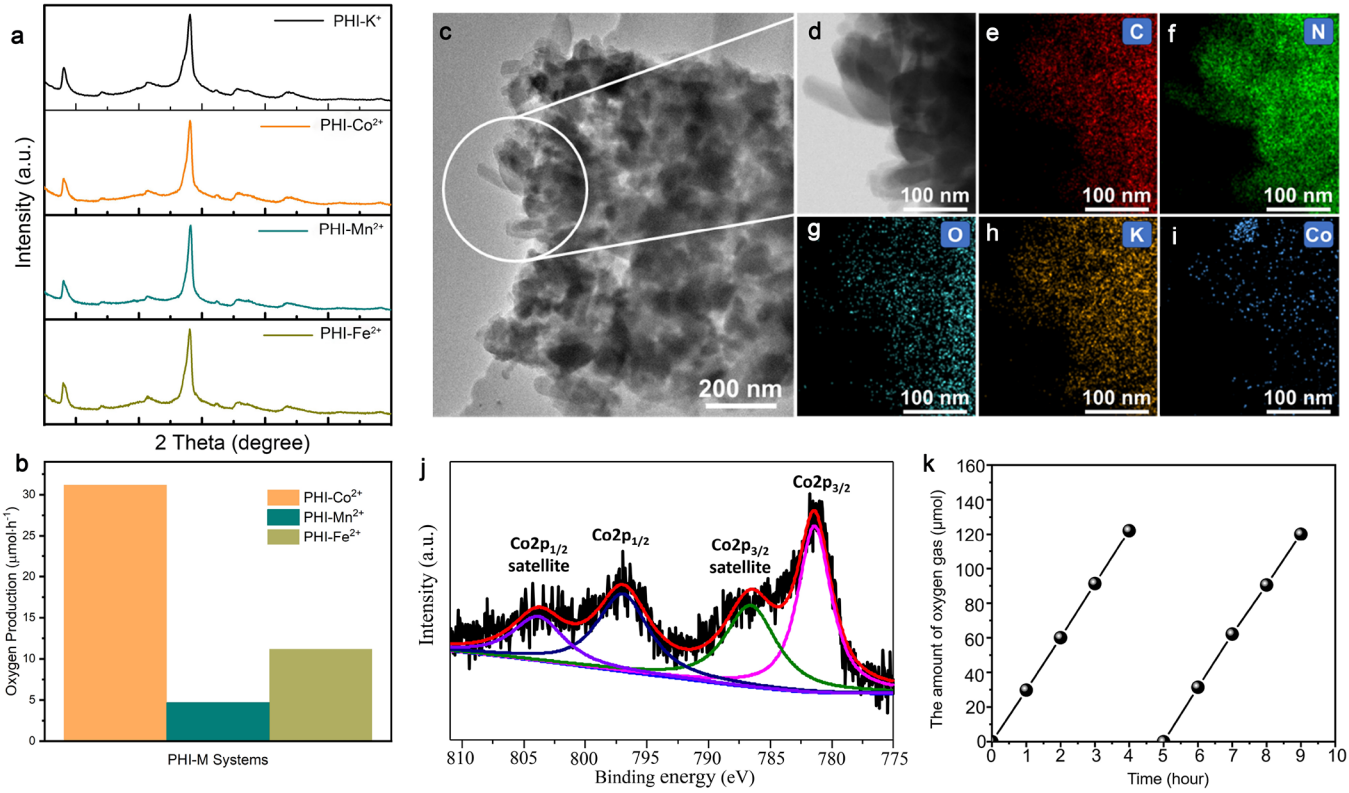

Figure 6. (a) PXRD patterns for the PHI-M. (b) Photocatalytic oxygen production rate collected under $\lambda \geq 420$ nm of the tested PHI-M (0.41 wt % PHI-Co^{2+}, 3.1 wt % PHI-Fe^{2+}, and 0.33 wt % PHI-Mn^{2+}). For reference, no OER activity was detected for PHI-K+. More detailed data with different metal contents can be found in Table S3. (c) TEM image of PHI-Co^{2+} photocatalyst. (d) HAADF image showing the corresponding elements (e) carbon, (f) nitrogen, (g) oxygen, (h) potassium, and (i) cobalt. (j) XPS analysis of the PHI-Co^{2+} system. (k) The measurements of the photocatalytic oxygen evolution reaction by PHI-Co^{2+} for two cycles with 8 h.

Experimental Validation toward PHI-M Photocatalysts with Prominent OER Activities. The doped PHIs, i.e., PHI-Co^{2+}, PHI-Fe^{2+}, PHI-K^{+}, and PHI-Mn^{2+}, were further prepared. Their respective PXRD patterns reported in Figure 6a show two main peaks at 8 and 27° attributed to the periodicity of heptazine units within the layers and to the interplanar stacking of the polymer layers, respectively. These two peaks are observed for all PHI-M, indicating that the structure of the poly(heptazine imide) backbone is well preserved in all cases despite the intercalated ions being partially changed from K^{+} to transition metal cation. Figure 6b illustrates the highest O_2 production rates under visible light irradiation (λ> 420 nm) obtained for PHI-Co^{2+}, PHI-Mn^{2+}, and PHI-Fe^{2+} samples corresponding to the metal contents indicated in the figure caption, whereas PHI-K^{+} shows negligible OER activity in line with the predictions described above.

These experiments reveal that PHI-Co^{2+} photocatalysts exhibit much higher OER performance compared to PHI-Fe^{2+} and PHI-Mn^{2+} that show similar OER activity, in excellent agreement with the predicted trend. The resulting oxygen production for PHI-Co^{2+} (31.2 μmol·h^{-1}) is almost 60 times higher than the value previously reported for g-C_3N_4 (0.5 μmol·h^{-1}).[50] Remarkably, PHI-Co^{2+} surpasses WO_3/$BiVO_4$ catalysts (5 μmol·h^{-1})[68] while showing a similar level of performance to the OER catalysts including some perovskites such as $CaNbO_2N$ (40 μmol·h^{-1}).[45] Nonetheless, because of the straightforward method of obtaining the single atom doped PHI, this material stands as one of the most promising OER catalysts.

The best OER photocatalyst, PHI-Co^{2+}, was further characterized. The transmission electron microscopy (TEM) images of the sample are shown in Figure 6c. The elements carbon, nitrogen, oxygen, potassium, and cobalt are clearly visible (Figure 6e–i) in the high-angle annular dark-field (HAADF) images. It is noteworthy that cobalt is uniformly distributed on the surface of PHI, suggesting the involvement of cobalt in the framework of PHI. The Co 2p high-resolution spectrum in Figure 6j reveals two doublet peaks. The peaks at 781.3 and 796.8 eV are attributed to the Co 2p3/2 and 2p 2 signals, respectively. The other two peaks at binding energies of 786.4 and 803.8 eV are assigned to the corresponding satellite peaks. The X-ray photoelectron spectroscopy (XPS) observation suggests that Co forms as Co^{2+}. To further analyze the stability of this best catalyst, two cycles of photocatalytic oxygen evolution reactions were conducted by using PHI-Co^{2+}(Figure 6k). The system underwent revacuuming before each cycle to maintain pressure equilibrium. Throughout the 8 h measurements, no degradation was observed, indicating the outstanding stability of PHI-Co^{2+} in the OER.

CONCLUSIONS

A computational screening of a series of metal-ion-doped PHI-M was first conducted at the DFT level to identify the best OER catalysts. Through a detailed analysis of the electronic properties of this family of PHI-M and the Gibbs energy profile of the reaction pathway, PHI-Co^{2+} was predicted as the best candidate for catalytic OER. A rational analysis of the electronic properties of the intermediate species in the reaction

https://doi.org/10.1021/acscatal.3c05961
ACS Catal. 2024, 14, 2562−2571

pathway enabled us to unravel key descriptors that govern the OER activity of PHI-M, leading to the exploration of an alternative effective OER catalyst, i.e., PHI-Fe^{2+}. The same RDS and close energy barrier for PHI-Fe^{2+} and PHI-Mn^{2+} suggest a similar OER performance. Analysis of the excited states of the PHI-M systems by time-dependent DFT evidenced that doping with M^{2+} cations and in particular with Co^{2+} is an effective way to boost the photoactivity of this system due to an extension of the absorption energy region and to the population of long-lived charge separated states upon VIS light irradiation. The predicted PHI-Co^{2+}, PHI-Fe^{2+}, and PHI-Mn^{2+} were further synthesized, and their photocatalytic tests confirmed that PHI-Co^{2+} shows the highest level of performance with an oxygen production more than 60 times higher than the value previously reported for g-C_3N_4 (31.2 vs 0.05 $\mu mol \cdot h^{-1}$) while standing among the best OER catalysts as typical perovskites. Overall, this synergistic modeling-experimental effort appears to be an effective way to accelerate the tailoring of catalysts with improved OER activities, paving the way toward the development of effective catalysts without requiring time-consuming and tedious experimental testing.

■ ASSOCIATED CONTENT

Supporting Information

The Supporting Information is available free of charge at https://pubs.acs.org/doi/10.1021/acscatal.3c05961.

Simulation model, DFT and TD-DFT details, band position analysis, PDOS for different systems, contribution of different orbitals, reaction intermediates, ZPE and TS values, detailed reaction energies, absorption spectra, NTO plots, photocatalytic oxygen production, and Supporting Information references (PDF)

■ AUTHOR INFORMATION

Corresponding Authors

Markus Antonietti − *Department of Colloid Chemistry, Max Planck Institute of Colloids and Interfaces, Potsdam 14476, Germany*; orcid.org/0000-0002-8395-7558; Email: Markus.Antonietti@mpikg.mpg.de

Guillaume Maurin − *ICGM, Université de Montpellier, CNRS, ENSCM, Montpellier 34293, France*; orcid.org/0000-0002-2096-0450; Email: guillaume.maurin1@umontpellier.fr

Authors

Shanping Liu − *ICGM, Université de Montpellier, CNRS, ENSCM, Montpellier 34293, France*

Valentin Diez-Cabanes − *ICGM, Université de Montpellier, CNRS, ENSCM, Montpellier 34293, France*

Dong Fan − *ICGM, Université de Montpellier, CNRS, ENSCM, Montpellier 34293, France*

Lu Peng − *Department of Colloid Chemistry, Max Planck Institute of Colloids and Interfaces, Potsdam 14476, Germany*

Yuanxing Fang − *State Key Laboratory of Photocatalysis on Energy and Environment, College of Chemistry, Fuzhou University, Fuzhou 350116, P. R. China*; orcid.org/0000-0001-7603-5531

Complete contact information is available at: https://pubs.acs.org/10.1021/acscatal.3c05961

Notes

The authors declare no competing financial interest.

■ ACKNOWLEDGMENTS

The authors gratefully acknowledge the financial support provided by the METHASOL H2020-LC-SC3-RES-3-2020 project. The computational work was performed using HPC resources from GENCI-CINES (Grant A0140907613).

■ REFERENCES

(1) Kudo, A.; Miseki, Y. Heterogeneous photocatalyst materials for water splitting. *Chem. Soc. Rev.* **2009**, *38* (1), 253−278.

(2) Hisatomi, T.; Kubota, J.; Domen, K. Recent advances in semiconductors for photocatalytic and photoelectrochemical water splitting. *Chem. Soc. Rev.* **2014**, *43* (22), 7520−7535.

(3) Tachibana, Y.; Vayssieres, L.; Durrant, J. R. Artificial photosynthesis for solar water-splitting. *Nat. Photonics* **2012**, *6* (8), 511−518.

(4) Fujishima, A.; Honda, K. Electrochemical Photolysis of Water at a Semiconductor Electrode. *Nature* **1972**, *238* (5358), 37−38.

(5) Jang, E. S.; Won, J.-H.; Hwang, S.-J.; Choy, J.-H. Fine Tuning of the Face Orientation of ZnO Crystals to Optimize Their Photocatalytic Activity. *Adv. Mater.* **2006**, *18* (24), 3309−3312.

(6) Huang, W.-C.; Lyu, L.-M.; Yang, Y.-C.; Huang, M. H. Synthesis of Cu_2O Nanocrystals from Cubic to Rhombic Dodecahedral Structures and Their Comparative Photocatalytic Activity. *J. Am. Chem. Soc.* **2012**, *134* (2), 1261−1267.

(7) Hu, Y.; Gao, X.; Yu, L.; Wang, Y.; Ning, J.; Xu, S.; Lou, X. W. Carbon-Coated CdS Petalous Nanostructures with Enhanced Photostability and Photocatalytic Activity. *Angew. Chem., Int. Ed.* **2013**, *52* (21), 5636−5639.

(8) Iwashina, K.; Kudo, A. Rh-Doped $SrTiO_3$ Photocatalyst Electrode Showing Cathodic Photocurrent for Water Splitting under Visible-Light Irradiation. *J. Am. Chem. Soc.* **2011**, *133* (34), 13272−13275.

(9) Cao, S.-W.; Yin, Z.; Barber, J.; Boey, F. Y. C.; Loo, S. C. J.; Xue, C. Preparation of Au-$BiVO_4$ Heterogeneous Nanostructures as Highly Efficient Visible-Light Photocatalysts. *ACS Appl. Mater. Interfaces* **2012**, *4* (1), 418−423.

(10) Wang, X.; Maeda, K.; Thomas, A.; Takanabe, K.; Xin, G.; Carlsson, J. M.; Domen, K.; Antonietti, M. A metal-free polymeric photocatalyst for hydrogen production from water under visible light. *Nat. Mater.* **2009**, *8* (1), 76−80.

(11) Rosso, C.; Filippini, G.; Criado, A.; Melchionna, M.; Fornasiero, P.; Prato, M. Metal-Free Photocatalysis: Two-Dimensional Nanomaterial Connection toward Advanced Organic Synthesis. *ACS Nano* **2021**, *15* (3), 3621−3630.

(12) Wang, X.; Blechert, S.; Antonietti, M. Polymeric Graphitic Carbon Nitride for Heterogeneous Photocatalysis. *ACS Catal.* **2012**, *2* (8), 1596−1606.

(13) Ong, W.-J.; Tan, L.-L.; Ng, Y. H.; Yong, S.-T.; Chai, S.-P. Graphitic Carbon Nitride (g-C_3N_4)-Based Photocatalysts for Artificial Photosynthesis and Environmental Remediation: Are We a Step Closer to Achieving Sustainability? *Chem. Rev.* **2016**, *116* (12), 7159−7329.

(14) Ye, S.; Wang, R.; Wu, M.-Z.; Yuan, Y.-P. A review on g-C_3N_4 for photocatalytic water splitting and CO_2 reduction. *Appl. Surf. Sci.* **2015**, *358*, 15−27.

(15) Lam, S.-M.; Sin, J.-C.; Mohamed, A. R. A review on photocatalytic application of g-C_3N_4/semiconductor (CNS) nanocomposites towards the erasure of dyeing wastewater. *Mater. Sci. Semicond.* **2016**, *47*, 62−84.

(16) Zheng, Y.; Lin, L.; Wang, B.; Wang, X. Graphitic Carbon Nitride Polymers toward Sustainable Photoredox Catalysis. *Angew. Chem., Int. Ed.* **2015**, *54* (44), 12868−84.

(17) Tay, Q.; Kanhere, P.; Ng, C. F.; Chen, S.; Chakraborty, S.; Huan, A. C. H.; Sum, T. C.; Ahuja, R.; Chen, Z. Defect Engineered g-C_3N_4 for Efficient Visible Light Photocatalytic Hydrogen Production. *Chem. Mater.* **2015**, *27* (14), 4930−4933.

(18) Wang, Z.; Huang, Y.; Chen, M.; Shi, X.; Zhang, Y.; Cao, J.; Ho, W.; Lee, S. C. Roles of N-Vacancies over Porous g-C_3N_4 Microtubes during Photocatalytic NOx Removal. *ACS Appl. Mater. Interfaces* **2019**, *11* (11), 10651−10662.
(19) Nor, N. U. M.; Mazalan, E.; Amin, N. A. S. Insights into enhancing photocatalytic reduction of CO_2: Substitutional defect strategy of modified g-C_3N_4 by experimental and theoretical calculation approaches. *J. Alloys Compd.* **2021**, *871*, No. 159464.
(20) Fontelles-Carceller, O.; Munoz-Batista, M. J.; Fernandez-Garcia, M.; Kubacka, A. Interface Effects in Sunlight-Driven Ag/g-C_3N_4 Composite Catalysts: Study of the Toluene Photodegradation Quantum Efficiency. *ACS Appl. Mater. Interfaces* **2016**, *8* (4), 2617−27.
(21) Tian, S.; Wang, Z.; Gong, W.; Chen, W.; Feng, Q.; Xu, Q.; Chen, C.; Chen, C.; Peng, Q.; Gu, L.; Zhao, H.; Hu, P.; Wang, D.; Li, Y. Temperature-Controlled Selectivity of Hydrogenation and Hydrodeoxygenation in the Conversion of Biomass Molecule by the Ru1/mpg-C_3N_4 Catalyst. *J. Am. Chem. Soc.* **2018**, *140* (36), 11161−11164.
(22) Chu, Y.-C.; Lin, T.-J.; Lin, Y.-R.; Chiu, W.-L.; Nguyen, B.-S.; Hu, C. Influence of P, S, O-Doping on g-C_3N_4 for hydrogel formation and photocatalysis: An experimental and theoretical study. *Carbon* **2020**, *169*, 338−348.
(23) Zhao, D.; Wang, Y.; Dong, C.-L.; Huang, Y.-C.; Chen, J.; Xue, F.; Shen, S.; Guo, L. Boron-doped nitrogen-deficient carbon nitride-based Z-scheme heterostructures for photocatalytic overall water splitting. *Nat. Energy* **2021**, *6* (4), 388−397.
(24) Pramoda, K.; Gupta, U.; Chhetri, M.; Bandyopadhyay, A.; Pati, S. K.; Rao, C. N. Nanocomposites of C_3N_4 with Layers of MoS_2 and Nitrogenated RGO, Obtained by Covalent Cross-Linking: Synthesis, Characterization, and HER Activity. *ACS Appl. Mater. Interfaces* **2017**, *9* (12), 10664−10672.
(25) Chu, K.; Liu, Y. P.; Li, Y. B.; Guo, Y. L.; Tian, Y. Two-dimensional (2D)/2D Interface Engineering of a MoS_2/C_3N_4 Heterostructure for Promoted Electrocatalytic Nitrogen Fixation. *ACS Appl. Mater. Interfaces* **2020**, *12* (6), 7081−7090.
(26) Kessler, F. K.; Zheng, Y.; Schwarz, D.; Merschjann, C.; Schnick, W.; Wang, X.; Bojdys, M. J. Functional carbon nitride materials - design strategies for electrochemical devices. *Nat. Rev. Mater.* **2017**, *2* (6), 17030.
(27) Wang, W.; Shu, Z.; Zhou, J.; Tang, H.; Li, T.; Meng, D. Optimizing the Optical Absorption of Poly (heptazine imide) by the n → π^* Electron Transition for Improved Photocatalytic H_2 Evolution. *ACS Appl. Mater. Interfaces* **2022**, *14* (36), 41131−41140.
(28) Niu, P.; Yin, L. C.; Yang, Y. Q.; Liu, G.; Cheng, H. M. Increasing the visible light absorption of graphitic carbon nitride (melon) photocatalysts by homogeneous self-modification with nitrogen vacancies. *Adv. Mater.* **2014**, *26* (47), 8046−52.
(29) Rodriguez, N. A.; Savateev, A.; Grela, M. A.; Dontsova, D. Facile Synthesis of Potassium Poly (heptazine imide) (PHIK)/Ti-Based Metal-Organic Framework (MIL-125-NH_2) Composites for Photocatalytic Applications. *ACS Appl. Mater. Interfaces* **2017**, *9* (27), 22941−22949.
(30) Savateev, A.; Dontsova, D.; Kurpil, B.; Antonietti, M. Highly crystalline poly (heptazine imides) by mechanochemical synthesis for photooxidation of various organic substrates using an intriguing electron acceptor − Elemental sulfur. *J. Catal.* **2017**, *350*, 203−211.
(31) Markushyna, Y.; Teutloff, C.; Kurpil, B.; Cruz, D.; Lauermann, I.; Zhao, Y.; Antonietti, M.; Savateev, A. Halogenation of aromatic hydrocarbons by halide anion oxidation with poly (heptazine imide) photocatalyst. *Appl. Catal., B* **2019**, *248*, 211−217.
(32) Savateev, A.; Tarakina, N. V.; Strauss, V.; Hussain, T.; Ten Brummelhuis, K.; Sanchez Vadillo, J. M.; Markushyna, Y.; Mazzanti, S.; Tyutyunnik, A. P.; Walczak, R.; Oschatz, M.; Guldi, D. M.; Karton, A.; Antonietti, M. Potassium Poly (Heptazine Imide): Transition Metal-Free Solid-State Triplet Sensitizer in Cascade Energy Transfer and [3 + 2]-cycloadditions. *Angew. Chem., Int. Ed.* **2020**, *59* (35), 15061−15068.
(33) Kröger, J.; Jiménez-Solano, A.; Savasci, G.; Rovó, P.; Moudrakovski, I.; Küster, K.; Schlomberg, H.; Vignolo-González, H. A.; Duppel, V.; Grunenberg, L.; Dayan, C. B.; Sitti, M.; Podjaski, F.; Ochsenfeld, C.; Lotsch, B. V. Interfacial Engineering for Improved Photocatalysis in a Charge Storing 2D Carbon Nitride: Melamine Functionalized Poly (heptazine imide). *Adv. Energy Mater.* **2020**, *11* (6), 2003016.
(34) Wang, W.; Shu, Z.; Liao, Z.; Zhou, J.; Meng, D.; Li, T.; Zhao, Z.; Xu, L. Sustainable one-step synthesis of nanostructured potassium poly (heptazine imide) for highly boosted photocatalytic hydrogen evolution. *Chem. Eng. Sci.* **2021**, *424*, No. 130332.
(35) Savateev, A.; Pronkin, S.; Epping, J. D.; Willinger, M. G.; Wolff, C.; Neher, D.; Antonietti, M.; Dontsova, D. Potassium Poly (heptazine imides) from Aminotetrazoles: Shifting Band Gaps of Carbon Nitride-like Materials for More Efficient Solar Hydrogen and Oxygen Evolution. *ChemCatChem.* **2017**, *9* (1), 167−174.
(36) Savateev, A.; Kurpil, B.; Mishchenko, A.; Zhang, G.; Antonietti, M. A ″waiting″ carbon nitride radical anion: a charge storage material and key intermediate in direct C-H thiolation of methylarenes using elemental sulfur as the ″S″-source. *Chem. Sci.* **2018**, *9* (14), 3584−3591.
(37) Dontsova, D.; Pronkin, S.; Wehle, M.; Chen, Z.; Fettkenhauer, C.; Clavel, G.; Antonietti, M. Triazoles: A New Class of Precursors for the Synthesis of Negatively Charged Carbon Nitride Derivatives. *Chem. Mater.* **2015**, *27* (15), 5170−5179.
(38) Savateev, A.; Pronkin, S.; Willinger, M. G.; Antonietti, M.; Dontsova, D. Towards Organic Zeolites and Inclusion Catalysts: Heptazine Imide Salts Can Exchange Metal Cations in the Solid State. *Chem.—Asian J.* **2017**, *12* (13), 1517−1522.
(39) Sahoo, S. K.; Teixeira, I. F.; Naik, A.; Heske, J.; Cruz, D.; Antonietti, M.; Savateev, A.; Kühne, T. D. Photocatalytic Water Splitting Reaction Catalyzed by Ion-Exchanged Salts of Potassium Poly (heptazine imide) 2D Materials. *J. Phys. Chem. C* **2021**, *125* (25), 13749−13758.
(40) Wang, M.; Zhang, Z.; Chi, Z.; Lou, L.-l.; Li, H.; Yu, H.; Ma, T.; Yu, K.; Wang, H. Alkali Metal Cations as Charge-Transfer Bridge for Polarization Promoted Solar-to-H_2 Conversion. *Adv. Funct. Mater.* **2023**, *33* (9), 2211565.
(41) Huo, T.; Deng, Q.; Yu, F.; Wang, G.; Xia, Y.; Li, H.; Hou, W. Ion-Induced Synthesis of Crystalline Carbon Nitride Ultrathin Nanosheets from Mesoporous Melon for Efficient Photocatalytic Hydrogen Evolution with Synchronous Highly Selective Oxidation of Benzyl Alcohol. *ACS Appl. Mater. Interfaces* **2022**, *14* (11), 13419−13430.
(42) Lee, Y.; Suntivich, J.; May, K. J.; Perry, E. E.; Shao-Horn, Y. Synthesis and Activities of Rutile IrO_2 and RuO_2 Nanoparticles for Oxygen Evolution in Acid and Alkaline Solutions. *J. Phys. Chem. Lett.* **2012**, *3* (3), 399−404.
(43) Yu, J.; He, Q.; Yang, G.; Zhou, W.; Shao, Z.; Ni, M. Recent Advances and Prospective in Ruthenium-Based Materials for Electrochemical Water Splitting. *ACS Catal.* **2019**, *9* (11), 9973−10011.
(44) Bae, S.-Y.; Mahmood, J.; Jeon, I.-Y.; Baek, J.-B. Recent advances in ruthenium-based electrocatalysts for the hydrogen evolution reaction. *Nanoscale Horiz.* **2020**, *5* (1), 43−56.
(45) Wang, Y.; Jin, S.; Sun, X.; Wei, S.; Chen, L.; Xu, X. J. A. C. B. E. Switching on efficient photocatalytic water oxidation reactions over $CaNbO_2N$ by Mg modifications under visible light illumination. *Appl. Catal., B* **2019**, *245*, 10−19.
(46) Chen, J. Y. C.; Dang, L.; Liang, H.; Bi, W.; Gerken, J. B.; Jin, S.; Alp, E. E.; Stahl, S. S. Operando Analysis of NiFe and Fe Oxyhydroxide Electrocatalysts for Water Oxidation: Detection of Fe^{4+} by Mössbauer Spectroscopy. *J. Am. Chem. Soc.* **2015**, *137* (48), 15090−15093.
(47) Kandambeth, S.; Kale, V. S.; Fan, D.; Bau, J. A.; Bhatt, P. M.; Zhou, S.; Shkurenko, A.; Rueping, M.; Maurin, G.; Shekhah, O.; Eddaoudi, M. Unveiling Chemically Robust Bimetallic Squarate-Based Metal-Organic Frameworks for Electrocatalytic Oxygen Evolution Reaction. *Adv. Energy Mater.* **2023**, *13* (1), 2202964.
(48) Ye, M.; Li, S.; Zhao, X.; Tarakina, N. V.; Teutloff, C.; Chow, W. Y.; Bittl, R.; Thomas, A. Cobalt-Exchanged Poly (Heptazine Imides)

as Transition Metal-Nx Electrocatalysts for the Oxygen Evolution Reaction. *Adv. Mater.* **2020**, *32* (9), No. e1903942.
(49) Zhang, X.; Yu, C.; Guan, J.; Jiang, S.; Wang, Y.; Deng, K.; Meng, Z.; Lu, R. Polymeric heptazine imide by O doping and constructing van der Waals heterostructures for photocatalytic water splitting: a theoretical perspective from transition dipole moment analyses. *Phys. Chem. Chem. Phys.* **2020**, *22* (18), 9915−9922.
(50) Ajmal, Z.; Hayat, A.; Qasim, M.; Kumar, A.; El Jery, A.; Abbas, W.; Hussain, M. B.; Qadeer, A.; Iqbal, S.; Bashir, S.; Ahmad, Z.; Qian, J.; Murtaza, A.; Zeng, H. Technologies, Assembly of a novel Fe2TiO5-impregnated donor-π-acceptor conjugated carbon nitride for highly efficient solar water splitting. *Sustainable Mater. Technol.* **2023**, *36*, No. e00594.
(51) Savateev, A.; Pronkin, S.; Willinger, M. G.; Antonietti, M.; Dontsova, D. Towards Organic Zeolites and Inclusion Catalysts: Heptazine Imide Salts Can Exchange Metal Cations in the Solid State. *Chem.—Asian J.* **2017**, *12* (13), 1517−1522.
(52) Kresse, G.; Joubert, D. From ultrasoft pseudopotentials to the projector augmented-wave method. *Phys. Rev. B* **1999**, *59* (3), 1758−1775.
(53) Blöchl, P. E. Projector augmented-wave method. *Phys. Rev. B* **1994**, *50* (24), 17953−17979.
(54) Perdew, J. P.; Burke, K.; Ernzerhof, M. Generalized Gradient Approximation Made Simple. *Phys. Rev. Lett.* **1996**, *77* (18), 3865−3868.
(55) Grimme, S.; Ehrlich, S.; Goerigk, L. Effect of the damping function in dispersion corrected density functional theory. *J. Comput. Chem.* **2011**, *32* (7), 1456−1465.
(56) Wang, M.; Navrotsky, A. Enthalpy of formation of $LiNiO_2$, $LiCoO_2$ and their solid solution, $LiNi_{1-x}Co_xO_2$. *Solid State Ionics* **2004**, *166*, 167−173, DOI: 10.1016/j.ssi.2003.11.004.
(57) Nørskov, J. K.; Rossmeisl, J.; Logadottir, A.; Lindqvist, L.; Kitchin, J. R.; Bligaard, T.; Jónsson, H. Origin of the Overpotential for Oxygen Reduction at a Fuel-Cell Cathode. *J. Phys. Chem. B* **2004**, *108* (46), 17886−17892.
(58) Sun, J.; Ruzsinszky, A.; Perdew, J. P. Strongly Constrained and Appropriately Normed Semilocal Density Functional. *Phys. Rev. Lett.* **2015**, *115* (3), No. 036402.
(59) Heyd, J.; Scuseria, G. E.; Ernzerhof, M. Hybrid functionals based on a screened Coulomb potential. *J. Chem. Phys.* **2003**, *118* (18), 8207−8215.
(60) Henkelman, G.; Arnaldsson, A.; Jónsson, H. A fast and robust algorithm for Bader decomposition of charge density. *Comput. Mater. Sci.* **2006**, *36* (3), 354−360.
(61) Maintz, S.; Deringer, V. L.; Tchougréeff, A. L.; Dronskowski, R. LOBSTER: A tool to extract chemical bonding from plane-wave based DFT. *J. Comput. Chem.* **2016**, *37* (11), 1030−1035.
(62) Grimme, S. A simplified Tamm-Dancoff density functional approach for the electronic excitation spectra of very large molecules. *J. Chem. Phys.* **2013**, *138* (24), 244104.
(63) Crowley, J. M.; Tahir-Kheli, J.; Goddard, W. A. Resolution of the Band Gap Prediction Problem for Materials Design. *J. Phys. Chem. Lett.* **2016**, *7* (7), 1198−1203.
(64) Huang, J.; Lu, Y.; Zhang, H.; Shangguan, L.; Mou, Z.; Sun, J.; Sun, S.; He, J.; Lei, W. Template-free synthesis of mesh-like graphic carbon nitride with optimized electronic band structure for enhanced photocatalytic hydrogen evolution. *Chem. Eng. J.* **2021**, *405*, No. 126685.
(65) Suen, N.-T.; Hung, S.-F.; Quan, Q.; Zhang, N.; Xu, Y.-J.; Chen, H. M. Electrocatalysis for the oxygen evolution reaction: recent development and future perspectives. *Chem. Soc. Rev.* **2017**, *46* (2), 337−365.
(66) Dronskowski, R.; Bloechl, P. E. Crystal orbital Hamilton populations (COHP): energy-resolved visualization of chemical bonding in solids based on density-functional calculations. *J. Phys. Chem.* **1993**, *97* (33), 8617−8624.
(67) Peach, M. J.; Williamson, M. J.; Tozer, D. J. Influence of triplet instabilities in TDDFT. *J. Chem. Theory Comput.* **2011**, *7* (11), 3578−3585.
(68) Yan, J.; Wu, H.; Chen, H.; Zhang, Y.; Zhang, F.; Liu, S. F. Fabrication of TiO_2/C_3N_4 heterostructure for enhanced photocatalytic Z-scheme overall water splitting. *Appl. Catal., B* **2016**, *191*, 130−137.

https://doi.org/10.1021/acscatal.3c05961
ACS Catal. 2024, 14, 2562−2571